Supplementary Information for "Macroscopic Manifestation of Domain-wall Magnetism and Magnetoelectric Effect in a Néel-type Skyrmion Host"

K. Geirhos*,[1] B. Gross,[2] B. G. Szigeti,[1] A. Mehlin,[2] S. Philipp,[2] J. S. White,[3] R. Cubitt,[4] S. Widmann,[1] S. Ghara,[1] P. Lunkenheimer,[1] V. Tsurkan,[1,5] E. Neuber,[6] D. Ivaneyko,[6] P. Milde,[6] L. M. Eng,[6,7] A. O. Leonov,[8,9] S. Bordács,[10,11] M. Poggio,[2] and I. Kézsmárki[1]

[1]*Experimental Physics V, Center for Electronic Correlations and Magnetism, University of Augsburg, 86135 Augsburg, Germany*
[2]*Department of Physics, University of Basel, 4056 Basel, Switzerland*
[3]*Laboratory for Neutron Scattering and Imaging, Paul Scherrer Institut, CH-5232 Villigen, Switzerland*
[4]*Institut Laue-Langevin, 6 rue Jules Horowitz, 38042 Grenoble, France*
[5]*Institute of Applied Physics, Academy of Sciences of Moldova, MD 2028, Chisinau, Republica Moldova*
[6]*Institute of Applied Photophysics, University of Technology Dresden, 01062 Dresden, Germany*
[7]*ct.qmat, Dresden-Wrzburg Cluster of Excellence - EXC 2147, TU Dresden, 01062 Dresden, Germany*
[8]*Center for Chiral Science, Hiroshima University, Higashi-Hiroshima, Hiroshima, 739-8526, Japan*
[9]*Department of Chemistry, Faculty of Science, Hiroshima University Kagamiyama, Higashi-Hiroshima, Hiroshima, 739-8526, Japan*
[10]*Department of Physics, Budapest University of Technology and Economics, 1111 Budapest, Hungary*
[11]*Hungarian Academy of Sciences, Premium Postdoctor Program, 1051 Budapest, Hungary*

Contents:

1. Typical ferroelectric domain patterns in GaV_4Se_8

In Supplementary Figure 1 we show a typical ferroelectric domain pattern observed on the (001) surface of a cleaved GaV_4Se_8 crystal at $T = 10$ K. The topography is characterized by two distinct patterns: The dense stripes roughly parallel to the [110] axis are introduced by cleavage of the sample; in contrast, the folds parallel to the [010] axis are typical for ferroelastic lamellar domains and have also been observed on the parent compounds GaV_4S_8[1] as well as $GaMo_4S_8$[2]. They originate from the differently oriented distortion of ferroelastic domains.

The polar axis in GaV_4Se_8 is parallel to a $\langle 111 \rangle$ axis. Hence, on the (001) plane neighboring domains separated by mechanically and electrically compatible domain walls share the same in-plane polarization component but are characterized by an alternating out-of-plane polarization component[2]. The resulting alternating surface charge provokes a distinct contrast in the dissipation channel of the nc-AFM, where every second domain appears bright. Since we used a non-magnetic PtSi-tip, a magnetic origin of dissipation contrast can readily be excluded here. At the same time, the polarization also causes contrast in the contact potential measured with KPFM simultaneously to the topography. The alternating surface charge leads to a contrast of about $\Delta U_{cpd} \approx 45$ mV between the two type of domains, while the uniform in-plane polarization manifests in the potential slope of $U'_{cpd} = 260 \sim \mathrm{mV\ \mu m^{-1}}$. With this compilation of real-space imaging measurements we have shown that GaV_4Se_8 forms similar polar domain arrangements as observed in GaV_4S_8 and $GaMo_4S_8$, consisting of pairs of domains forming long lamellar-like patterns.

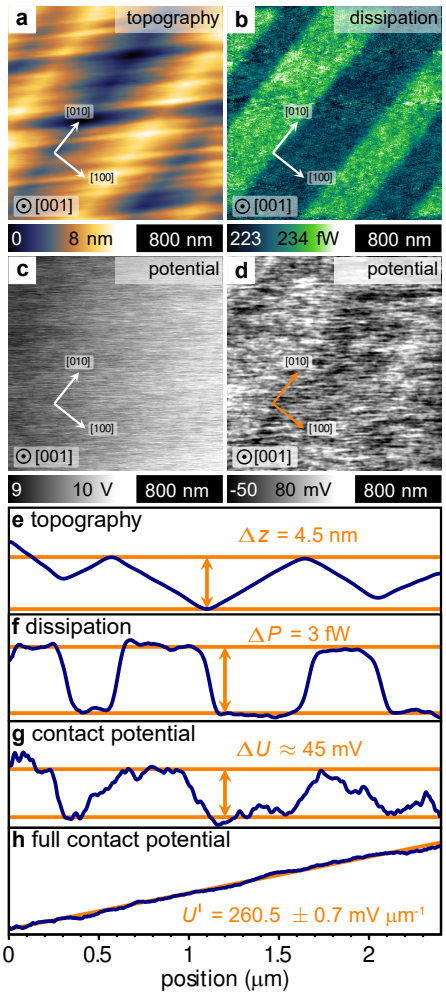

Supplementary Figure 1: | **Typical ferroelectric domain pattern observed on the (001) cleaved GaV_4Se_8 crystal surface at T=10 K. a,** The topography is characterized by stripes roughly parallel to the [110] axis and folds parallel to the [010] axis. The latter originate in the differently oriented distortion of the ferroelastic domains. The color scale corresponds to the z-displacement of the tip. **b,** In the dissipation channel of the nc-AFM every second domain appears bright. For the non-magnetic tip the dissipation originates from electric interactions. The dissipated power is indicated by the color scale. **c & d,** Surface potential measured via Kelvin-probe force microscopy simultaneously to the topography. In **c** a slope of the potential roughly along the [100] axis is visible. After subtraction of a plane, in **d** also the domain contrast becomes visible. In **c** the color scale corresponds to the overall change of the potential, while in **d** gives the local variation of the potential after subtracting the overall slope. **e - h,** Profiles from averaging the images **a-d** along the [010] axis. The out-of-plane component of the polarization leads to the contrast in the dissipation channel as well as the contact potential, whereas the homogeneous in-plane polarization component causes the slope in the contact potential. The surface folds originate in ferroelastic distortions.

2. Angular dependence of magneto-current for the P_2 mono-domain state

In all magneto-current measurements shown within this work the current along the direction of the polar axis of P_1 is detected. Therefore, different mixtures of the components of the polarization being parallel ($P_\parallel$) and perpendicular ($P_\perp$) to the polar axes are probed for the four different domains. For P_1 domain exclusively the parallel component of the associated polarization is measured, whereas for domains P_{2-4} the measured polarization consists of 33% of the $P_\parallel$-component and up to 94% of the $P_\perp$-component. To exclude that the anomalies seen in multi-domain samples and assigned to DW transitions are not bulk transitions in $P_\perp$, angular dependent magneto-current measurements were performed in a nearly mono-domain P_2 state.

To achieve a mono-domain P_2 state, a magnetic field $\mu_0 H_\mathrm{p} = 14\,\mathrm{T}$ parallel to the polar axis of the domain P_2, which leads to the enhanced formation of P_2 domain, is applied during cooling of the samples through the JT transition from 50 K to 12 K. Since, P_1 domain is already predominant without any poling, in addition an electric field $E_\mathrm{p} = 2.1\,\mathrm{kV\ cm^{-1}}$ anti-parallel to polar axis of the P_1 domain was applied, which suppresses the formation of P_1 domain (Supplementary Figure 2b).

The dominance of the P_1 domain in an unpoled state can also clearly be seen in Supplementary Figure 2 d where the temperature dependence of the polarization as measured along the polar P_1 axis for different polings is shown. The polarization in an unpoled state saturates already at a high positive value of approximately $1.2\,\mu\mathrm{C\ cm^{-2}}$, which is even increased to $2.1\,\mu\mathrm{C\ cm^{-2}}$ when the crystal is poled with an positive electric field and a nearly P_1 mono-domain state is achieved. In contrast, poling with negative electric combined with magnetic fields leads to a negative polarization which at low temperatures reaches a value of approximately $-0.7\,\mu\mathrm{C\ cm^{-2}}$. This value also coincides with the polarization values expected for a P_2 mono-domain state, which is $-\frac{1}{3}$ of the polarization value of the P_1 mono-domain state.

The successful poling to the nearly P_2 mono-domain state can also be seen in the angular dependence of the magneto-current at 12 K in Supplementary Figure 2 a. While the anomalies associated with bulk magnetic transitions on the P_1 domains are absent except a faint trace of the SkL to FM transition around 0°, the anomalies associated with magnetic transitions on the P_2 are clearly seen. Also the anomaly solely seen in multi-domain samples located around 100 mT in the vicinity of (100) direction (54°) is absent (Supplementary Figure 2 c) excluding that this anomaly stems from a bulk transition in $P_\perp$.

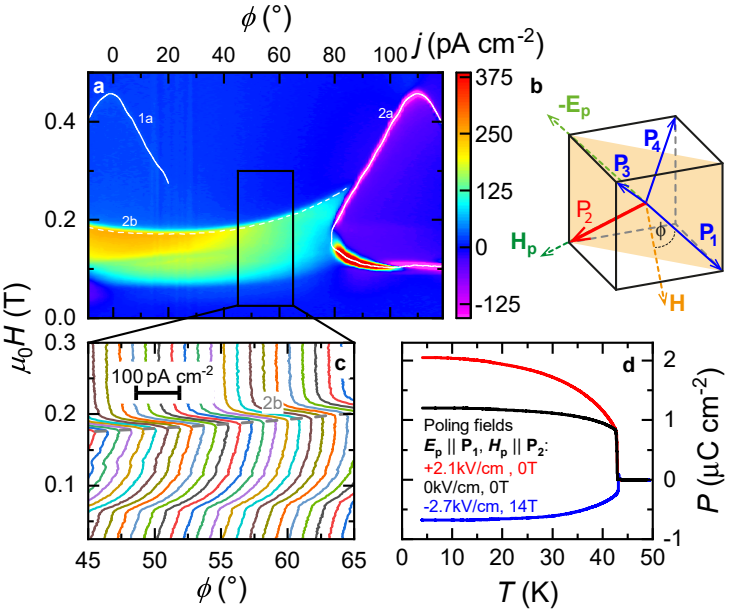

Supplementary Figure 2: |**Angular dependence of magneto-current for the P_2 mono-domain state at 12 K. a**, Colour map of the magneto-current density as a function of angle (ϕ) and magnitude (H) of the magnetic field for a nearly P_2 mono-domain state measured on sample # 2 at 12 K. The anomalies observed are highlighted by white lines and labeled according to the conventions introduced in Figure 4 of the main paper. **b**, Schematic representation of the cubic unit cell indicating the four possible directions of the polarization P_{1-4}, emerging in the rhombohedral phase. The directions of the applied poling fields ($\mathbf{H_p}$, $\mathbf{E_p}$) are indicated as well as the $(1\bar{1}0)$ plane in which the magnetic field was rotated by the angle ϕ for the measurement shown in panel a. Panel **c** shows a magnified view of the frame indicated in panel a, as a waterfall diagram, where the magneto-current curves recorded at different angles are shifted horizontally in proportion to ϕ. The temperature dependence of the polarization along the [111] axis after poling with different fields for sample # 2 is shown in panel **d**.

3. Comparison of angular dependence of magneto-current for different domain populations

Supplementary Figure 3 shows a comparison of the angular dependence of the magento-current for different domain populations. As seen in Supplementary Figure 5 of the main paper, a droplet-like Nel-type Skyrmion lattice state is present for a magnetic field spanning an angular range of 0° up to ∼ 30° with the polar axis and a transition from the cycloidal to the ferromagnetic state can be observed for a magnetic field spanning angles from ∼ 20° up to 90°. In accordance with this, anomalies associated with these phase transitions can be seen at the corresponding angles in the angular dependence of the magneto-current density on a nearly P_1 mono domain sample (Supplementary Figure 3a). The same anomalies mirrored at 54° can be also seen in a P_2 mono-domain state (Supplementary Figure 3 b), since the angle ϕ in all shown measurements is measured between the magnetic field and the P_1 polar axis and the angle separating the polar axes of P_1 and P_2 is 109° . Consequently, in the multi-domain state anomalies from both domains, P_1 and P_2 are present. In addition, two more anomalies associated with a transition within the DWs can be found in the multi-domain state around 100 mT crossing each other at 54° and extending over the entire angular range (Supplementary Figure 3 c and d).

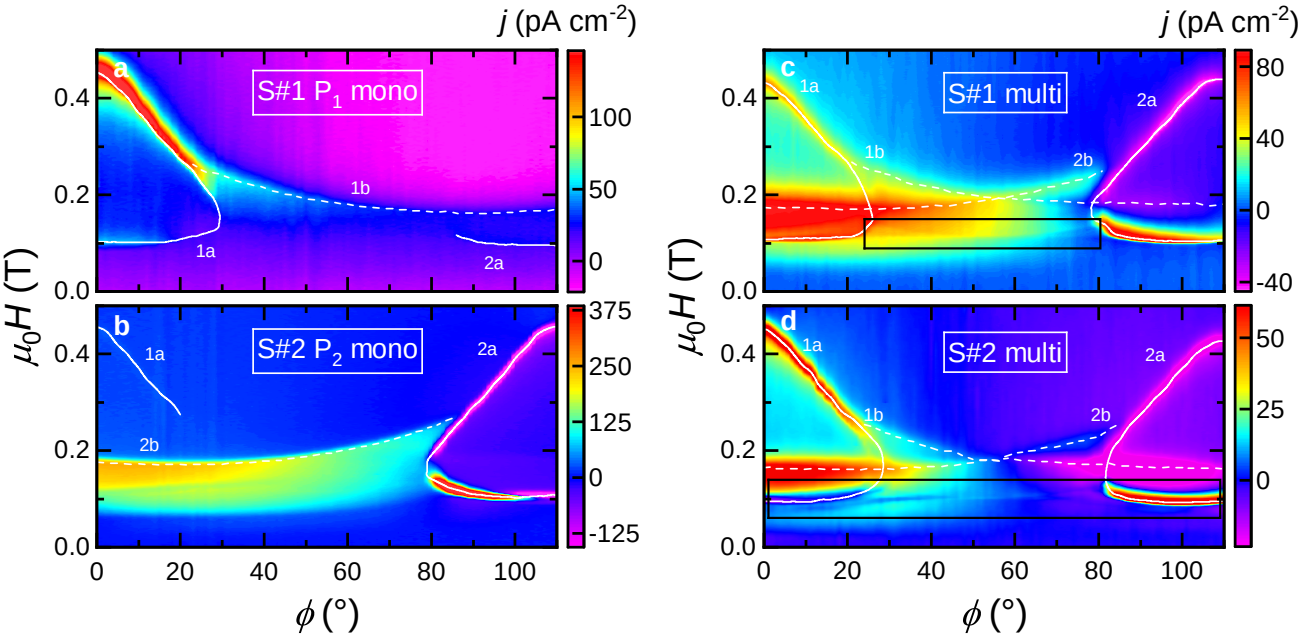

Supplementary Figure 3: |**Comparison of angular dependence of magneto-current for different domain populations at 12 K.** Colour maps of the magneto-current density as a function of angle (ϕ) between magnetic field and the polar axis of P_1 and magnitude (H) of the magnetic field for different domain populations. **a**, nearly P_1 mono-domain state measured on sample # 1. **b**, nearly P_2 mono-domain state measured on sample # 2. **c & d**, multi-domain state measured on samples #1 and # 2, respectively. The anomalies observed are highlighted by white lines and labelled according to the convections introduced in Supplementary Figure 4 of the main paper. The black boxes shown in panels c and d highlight the angle and field range in which anomalies associated with the DW transition can be observed.

4. Cycloidal q-vector reorientation

The magnetic-field-induced reorientation of the cycloidal domains is studied by small angle neutron scattering (SANS). The magnetic field dependence of the angular distribution of the scattered intensity is shown in Supplementary Figure 4 for **H** ‖[001]. The q-vectors corresponding to the cycloids of the P_1 domain point to the $\langle 1\bar{1}0\rangle$-type directions within the (111) plane. The in-plane component of the field, $\mathbf{H}_\perp$ ‖ $[11\bar{2}]$ rotates the cycloids toward the perpendicular $[1\bar{1}0]$ direction. Above ∼ 40 mT all intensities are collected into two spots around γ=0° and 180°, i.e. a cycloidal mono-domain state is realized.

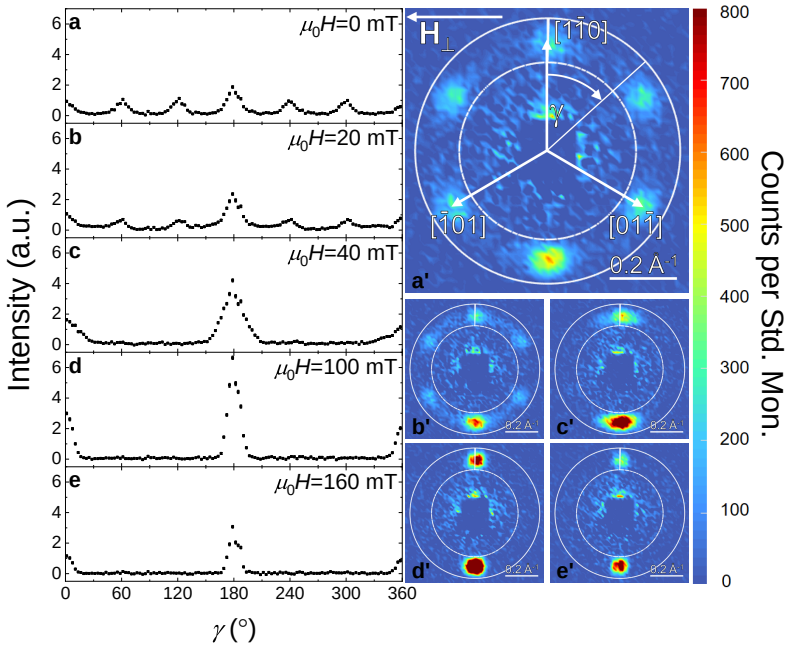

Supplementary Figure 4: | **Reorientation of the cycloidal q-vectors in GaV_4Se_8 at 12 K as traced by SANS. a-e,** Evolution of the azimuthal distribution of scattering intensity in the (111) plane as a function of magnetic field applied along the [001] direction. The azimuthal angle γ is measured from the $[1\bar{1}0]$ direction (see **a'**). The scattering images **a'-e'**, corresponding to the azimuthal intensity distributions in panels **a-e**, show the intensity pattern over the (111) plane. The intensity was integrated radially in the ring-like areas with white contours to get the azimuthal in-plane intensity distributions in **a-e**. In panel **a'**, the orientation of $H_\perp$ is shown.

Supplementary Figure 5 shows the cycloidal q-vector reorientation as recorded by magneto-current and magnetic susceptibility measurements. The q-vector reorientation is manifested as a peak in the magneto-current as well as in the susceptibility around 0.05 T. This reorientation only takes place the first time the magnetic field is increased after zero-field cooling and is not seen in consecutive magnetic field sweeps. This anomaly associated with the q-vector reorientation is clearly separated from the other anomalies, associated with magnetic phase boundaries.

Supplementary Figure 5: | **Signature of the cycloidal q-vector reorientation in magneto-current and magnetization data. a,** Magneto-current density of a polar mono-domain and **b,** magnetic susceptibility of a polar multi-domain sample with magnetic field applied along the [100] axis at 12 K after zero field cooling. In case of the magneto-current, two consecutive runs with increasing field are shown. The peak observed at ∼ 50 mT only in the first run, originates from the q-vector reorientation. The susceptibility is shown for increasing and consecutive decreasing field. The difference between the two is again assigned to the reorientation of the q-vectors. On the other hand, the peak at 100 mT, associated to magnetic states confined to the polar DWs, shows no hysteresis.

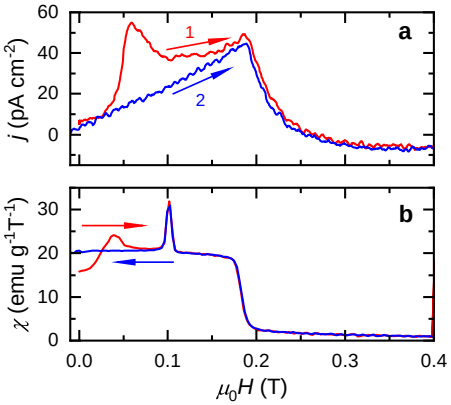

5. Magnetization step associated with magnetic states confined to DWs

Supplementary Figure 6 shows the change in the magnetization upon the transition from cycloidal to SkL state (anomaly at $\sim$ 80 mT in the green curve) in comparison with the weak anomaly at $\sim$100 mT, associated with a transition of the DW-confined magnetic states. The corresponding magnetization step in the second case is about 20 times weaker than in the former one.

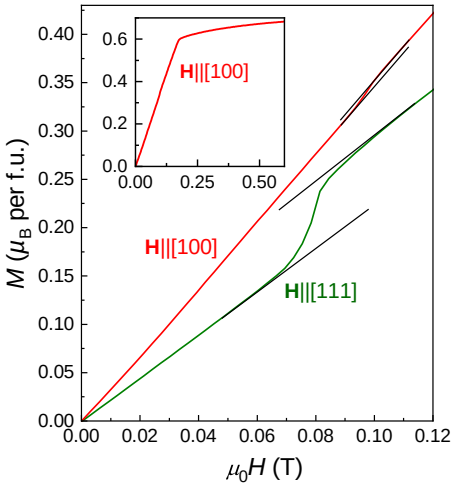

Supplementary Figure 6: | **Changes in the magnetization upon the cycloidal to SkL transition and upon the transition associated with magnetic states at the DWs.** Magnetization measured along the [111] axis (green curve) and the [100] axis (red curve) at 12 K. The black lines represent linear extrapolations of the magnetization in the neighbouring phases.

6. Possible scenario of the formation of magnetic states at the polar DWs

In the polar lacunar spinels GaV_4S_8, GaV_4Se_8 and $GaMo_4S_8$, the planar DWs connecting P_1 and P_2 domains are formed parallel to (001) planes. Similarly, DWs connecting P_1-P_4 and P_2-P_3 domains are parallel to (100) (see Supplementary Figure 7b), while DWs connecting P_1-P_3 and P_2-P_4 domains are parallel to (010) planes, as shown in Supplementary Figure 7c. The formation of the DWs in this fashion ensures both mechanical compatibility and electric neutrality at the DWs[2,3].

In Supplementary Figure 3d in the main text, two anomalies can be associated with the transition of magnetic states confined to the polar DWs. These two anomalies appear as a single phase boundary in Supplementary Figure 4 b of the main text, when the angle of the magnetic field is measured in one case from the P_1 and in the other case from the P_2 polar axis. This clearly shows that these two polar domains are involved in the DWs, where the magnetic edge states emerge. However, the fact that the anomaly originating from the magnetic states forming at the DWs can be observed at two magnetic field values for a given angle of the field, leads to the conclusion that the observed anomalies can stem from DWs connecting the P_1 domain to P_3 or P_4 domains and from DWs connecting the P_2 domain to P_3 or P_4 domains, but not from DWs connecting P_1 and P_2 domains.

For the magnetic field applied along the [001] axis, the field is parallel to all the four P_1-P_3, P_1-P_4, P_2-P_3 and P_2-P_4 DWs, but perpendicular to the P_1-P_2 and the P_3-P_4 DWs. For a general direction of the magnetic field within the $(1\bar{1}0)$ plane, the equivalency of the four DWs (P_1-P_3, P_1-P_4, P_2-P_3 and P_2-P_4) does not hold any more. While the magnetic field still spans the same angle with all the four DWs and also with the P_3 and P_4 polar axes, it spans different angles with the P_1 and P_2 polar axes. Correspondingly, for an arbitrary field direction in this plane, only the P_1-P_3 and the P_1-P_4 DWs are equivalent, as well as the P_2-P_3 and the P_2-P_4 DWs. This leads to a splitting of the anomaly observed at 100 mT for $\mathbf{H} \parallel [001]$ ($\phi = 54°$) into two separate anomalies, namely *1** and *2**, when the magnetic field is rotated away from this direction, as clear from Supplementary Figure 7d.

In the following, we outline a possible scenario for the formation of magnetic edge states at the DWs, e.g., those connecting the P_1 and P_3 domains. Two neighbouring P_1 and P_3 domains with their corresponding polarizations are shown in Supplementary Figure 7e. To ensure the charge neutrality of the DW, the polarization component normal to the DW is the same in the two adjacent domains and only the component lying in the plane of the DW changes. In GaV_4Se_8, the polar distortion activates the Dzyaloshinskii-Moriya interaction (DMI), leading to the formation of a cycloidal magnetic order with possible q-vectors perpendicular to the polar axis. Correspondingly, the DMI and the spin rotation plane of the cycloid change at the polar DW. The smooth matching of the spin cycloids at the DW requires a gradual rotation of the cycloidal plane. Moreover, the competition between the DMI within the adjacent domains leads to a reduced effective DMI in the vicinity of the DW. In finite magnetic fields, when the conical state is formed, this leads to a smaller cone angle in the vicinity of the DW and, thus, a lower critical field for the conical to FM transition. More specifically, when the magnetic field is applied along the [001] axis, the field spans an oblique angle with P_1 and P_3 polar axes and the cycloids in both domains distort into tilted conical structures [4], with a cone angle of α. On the other hand, this orientation of the field leads to a purely transverse conical state at the DW, with a cone angle of α' smaller than α (see the corresponding sketch in Supplementary Figure 7 e). For this reason, smaller magnetic fields are sufficient to close the cone and drive the system to the FM state at the DW as compared to the interior of the domain.

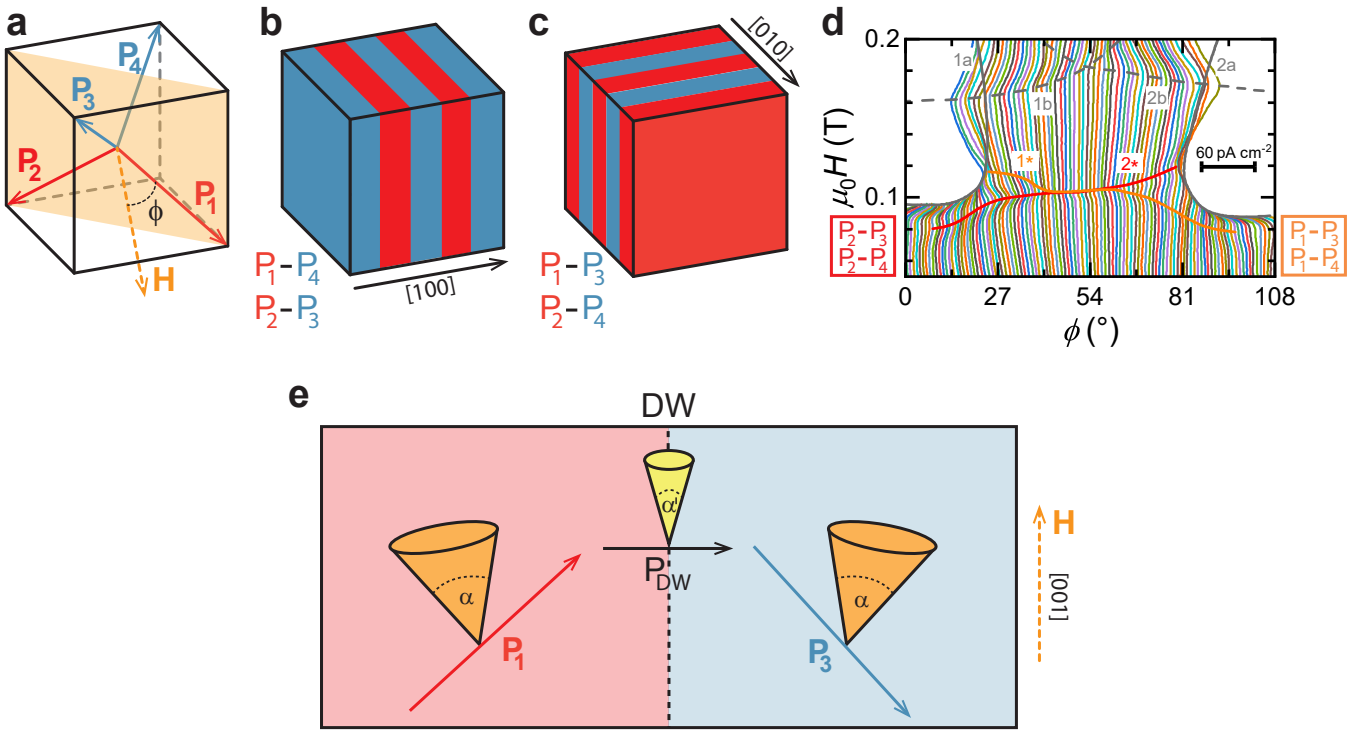

Supplementary Figure 7: | **Possible explanation for the DW phase boundary.** Schematic representations of the cubic unit cell indicating the four possible directions of the polarization, P_{1-4} (**a**) and the orientation of the DW planes for DWs between P_1-P_4 and P_2-P_3 (**b**) and P_1-P_3 and P_2-P_4 (**c**). In the magneto-current and the magnetic torque measurements, the magnetic field was rotated in the orange $(1\bar{1}0)$ plane, the angle ϕ is spanned by the magnetic field and the [111] axis (**a**). **d**, Repetition of Supplementary Figure 3d from the main text showing the angular dependent magneto-current data. In addition, the assignment of the anomalies, observed exclusively in the multi-domain samples, to the different DWs is given. **e**, Schematic sketch of the evolution of the conical structure throughout the DW.

References

[1] Kézsmárki, I. *et al.* Néel-type skyrmion lattice with confined orientation in the polar magnetic semiconductor GaV_4S_8. *Nat. Mater.* **14**, 1116–1122 (2015).

[2] Neuber, E. *et al.* Architecture of nanoscale ferroelectric domains in $GaMo_4S_8$. *J. Phys.-Condens. Mat.* **30**, 445402 (2018).

[3] Butykai, Á. *et al.* Characteristics of ferroelectric-ferroelastic domains in Néel-type skyrmion host GaV_4S_8. *Sci. Rep.* **7**, 44663 (2017).

[4] Bordács, S. *et al.* Equilibrium skyrmion lattice ground state in a polar easy-plane magnet. *Sci. Rep.* **7**, 7584 (2017).